PNAS RESEARCH ARTICLE | EARTH, ATMOSPHERIC, AND PLANETARY SCIENCES

Milankovitch cycles in banded iron formations constrain the Earth–Moon system 2.46 billion years ago

Margriet L. Lantink[a,1,2], Joshua H. F. L. Davies[b,c], Maria Ovtcharova[b], and Frederik J. Hilgen[a]

Edited by Linda Hinnov, George Mason University; received September 17, 2021; accepted August 22, 2022 by Editorial Board Member John W. Valley

The long-term history of the Earth–Moon system as reconstructed from the geological record remains unclear when based on fossil growth bands and tidal laminations. A possibly more robust method is provided by the sedimentary record of Milankovitch cycles (climatic precession, obliquity, and orbital eccentricity), whose relative ratios in periodicity change over time as a function of a decreasing Earth spin rate and increasing lunar distance. However, for the critical older portion of Earth's history where information on Earth–Moon dynamics is sparse, suitable sedimentary successions in which these cycles are recorded remain largely unknown, leaving this method unexplored. Here we present results of cyclostratigraphic analysis and high-precision U–Pb zircon dating of the lower Paleoproterozoic Joffre Member of the Brockman Iron Formation, NW Australia, providing evidence for Milankovitch forcing of regular lithological alternations related to Earth's climatic precession and orbital eccentricity cycles. Combining visual and statistical tools to determine their hierarchical relation, we estimate an astronomical precession frequency of 108.6 ± 8.5 arcsec/y, corresponding to an Earth–Moon distance of 321,800 ± 6,500 km and a daylength of 16.9 ± 0.2 h at 2.46 Ga. With this robust cyclostratigraphic approach, we extend the oldest reliable datum for the lunar recession history by more than 1 billion years and provide a critical reference point for future modeling and geological investigation of Precambrian Earth–Moon system evolution.

Earth–Moon system | Milankovitch cycles | Precambrian | banded iron formations | cyclostratigraphy

Significance

Milankovitch cycles recorded in 2.46-billion-year-old sediments indicate that Earth's precession cycle had a significantly higher frequency than present, signaling shorter daylengths and Earth–Moon distance. This result is based on the number of precession-scale cycles per orbital eccentricity cycle identified in the strata, and provides the oldest reliable geological datum constraining past Earth–Moon dynamics. The differences between then and now are due to tidal dissipation, which, on Earth, takes place largely in the oceans. Reconstruction of the long-term evolution of the Earth–Moon system has been subject of theoretical studies, but geological confirmation has been lacking especially early in Earth's history, where changes are most pronounced. Our study paves the way for future work bringing unprecedented insight into the Earth–Moon system history.

The past evolution of the Earth–Moon system is a major source of uncertainty in the history of our solar system. Over geologic time, Earth's spin velocity has decreased and the distance between the Earth and Moon has increased, due to tidal-induced dissipation of energy within Earth and the ocean (1). Extrapolation of the current rate of lunar recession of ∼3.8 cm/y back in time places the Moon at a close position to Earth as recently as 1.5 billion years ago (Ga) (2, 3). This timing is in direct conflict with the formation age of the Moon of around 4.5 Ga, based on radioisotopic dating of lunar rocks (4–6), implying that, over the course of Earth's history, the average tidal dissipation rate must have been much lower than present day. However, the details of this past evolution, and hence the corresponding trajectory of lunar recession, remain highly uncertain (7–14).

To provide constraints to models of Earth–Moon tidal evolution, empirical data from the geological record are needed. So far, these constraints have been mainly based on fossil growth bands revealing the number of daily growth increments per solar year (15) and tidal rhythmites revealing the number of tidal laminae per lunar month (16, 17). However, both these approaches have limitations, as it is challenging to find suitable records and to establish the exact number of growth bands/laminae. Fossil growth increment counts may be further complicated by a poor expression of the annual envelope, and these records are essentially absent before the Phanerozoic, with the exception of stromatolites (18, 19). While tidal deposits are not restricted to Phanerozoic times, sufficiently long and vertically accreted sequences that accurately document relevant paleotidal information have proven to be rare in the Precambrian. In addition, such tidal rhythmites are frequently plagued by incomplete laminae preservation during periods of low tidal amplitude at neap tide (17).

An alternative and potentially more robust method for constraining past Earth–Moon dynamics is based on the ratio between the periodicities of Earth's orbital eccentricity cycles and the climatic precession or obliquity cycles. These so-called "Milankovitch cycles," which cause quasi-periodic changes in insolation that, in turn, result in climate variations, are preserved as cyclic stratigraphic patterns ("cyclostratigraphy") in sedimentary strata. Importantly, the periods of the climatic precession and obliquity cycles (presently ∼21 and ∼41 ky, respectively) partly depend on the precession frequency of Earth's spin axis (astronomical precession frequency p), which is, in turn, directly related to the Earth–Moon system, where p decreases with increasing Earth–Moon distance and daylength. In contrast, the periods of the short and long eccentricity cycles of Earth's

Author contributions: M.L.L., J.H.F.L.D., and F.J.H. designed research; M.L.L., J.H.F.L.D., M.O., and F.J.H. performed research and analyzed data; and M.L.L., J.H.F.L.D., and F.J.H. wrote the paper.

The authors declare no competing interest.

This article is a PNAS Direct Submission. L.H. is a guest editor invited by the Editorial Board.

See online for related content such as Commentaries.

[1]To whom correspondence may be addressed. Email: lantink@wisc.edu.

[2]Present address: Department of Geoscience, University of Wisconsin–Madison, Madison, WI 53706.

This article contains supporting information online at http://www.pnas.org/lookup/suppl/doi:10.1073/pnas.2117146119/-/DCSupplemental.

Published September 26, 2022.

orbit (~100 and 405 ky, respectively) are independent of p and have remained largely stable throughout geologic time (20–22). In theory, the past evolution of the Earth–Moon system can therefore be reconstructed from the changing ratio between the Milankovitch cycle periods, assuming that there are sedimentary successions in which these cycles are well recorded.

For the more recent parts of the geological record, exceptional records of Milankovitch forcing have been identified in a wide range of depositional settings (from deep marine to lacustrine) where sedimentation occurred under relatively quiet and stable conditions over long intervals of time [i.e., millions of years (23)]. These well-preserved Phanerozoic records have been analyzed using cyclostratigraphic approaches to determine changes in past values of p (24–30). Unfortunately, high-quality records that have been unequivocally linked to Milankovitch forcing become increasingly scarce deeper in geological time, especially since the Milankovitch cyclicities need to be independently verified by high-precision geochronology. Thus far, the oldest cyclostratigraphic reconstruction combining independent age control with statistical analysis of the cycles comes from a relatively short stratigraphic section in *ca.* 1.4-Ga strata (27, 31). However, to determine the longer-term evolution and earlier history of the Earth–Moon system and/or tidal dissipation, robust data from much older time intervals are essential.

Banded iron formations (BIFs) are conspicuously layered marine deposits that primarily occur in the older parts of the Precambrian (32) and are a potential candidate for providing estimates of the changing Earth–Moon distance and daylength in deep time. Regular 5-m-scale alternations in the *ca.* 2.47-Ga Kuruman Iron Formation (IF) in South Africa (33) and the time-equivalent Dales Gorge Member of the Brockman IF in Western Australia (34) were recently linked to the 405-ky orbital eccentricity cycle through high-precision U–Pb geochronology and statistical analysis (33). The observed imprint of the 405-ky cycle implies the direct influence of climatic precession, since the main effect of orbital eccentricity on variations in solar insolation is through the amplitude modulation of the precession cycle (33). Accordingly, regular 15-cm-thick lithological alternations (the "Calamina cyclothem") (35) in the Dales Gorge Member hint at the presence of cyclicity at the scale of climatic precession in certain intervals (33, 34). Particularly promising, however, is the slightly younger Joffre Member of the Brockman IF, with distinct regular alternations on both the 10-cm (the "Knox cyclothem") and "65- to 150-cm" scales (35, 36), suggesting that both climatic precession and short (~100 ky) eccentricity have been recorded. In addition, the Joffre Member contains multiple zircon-bearing shaley intervals suitable for high-precision U–Pb dating (37).

Here, we present a detailed cyclostratigraphic study of the Joffre Member as exposed in a ~47-m-thick stratigraphic interval at Joffre Falls in the Karijini National Park, Hamersley Range, NW Australia (*SI Appendix*, Figs. S1 and S2), combined with high-precision U–Pb ages from Joffre Falls and a longer core intersecting the Joffre Member (DD98SGP001) ~150 km to the west. Our main research objective is twofold, namely, 1) to test the Milankovitch hypothesis for the Joffre Member strata at Joffre Falls and 2) to retrieve an accurate and precise value for the precession frequency p by evaluating and applying various statistical- and visual-based techniques. From this value, an Earth–Moon distance and length of day (LOD) can then be calculated. Finally, we compare our result with previously published geological estimates and theoretical models and discuss the implications for our understanding of Earth–Moon system tidal evolution.

Cyclostratigraphic Results from Joffre Falls. The outcrops of the Joffre Member at Joffre Falls exhibit a distinct hierarchy of regular alternations at a number of scales (Fig. 1). Viewed from a relative distance, prominent alternations are visible between reddish brown, indurated BIF and weathering-prone, thinner shaley intervals with a thickness of ~85 cm (Fig. 1*A*). On a larger (meter) scale, variations can be recognized in the thickness and distinctness of the shaley intervals (*SI Appendix*). Combined, the ~85-cm- and meter-scale alternations form a characteristic bundling pattern that is laterally continuous at

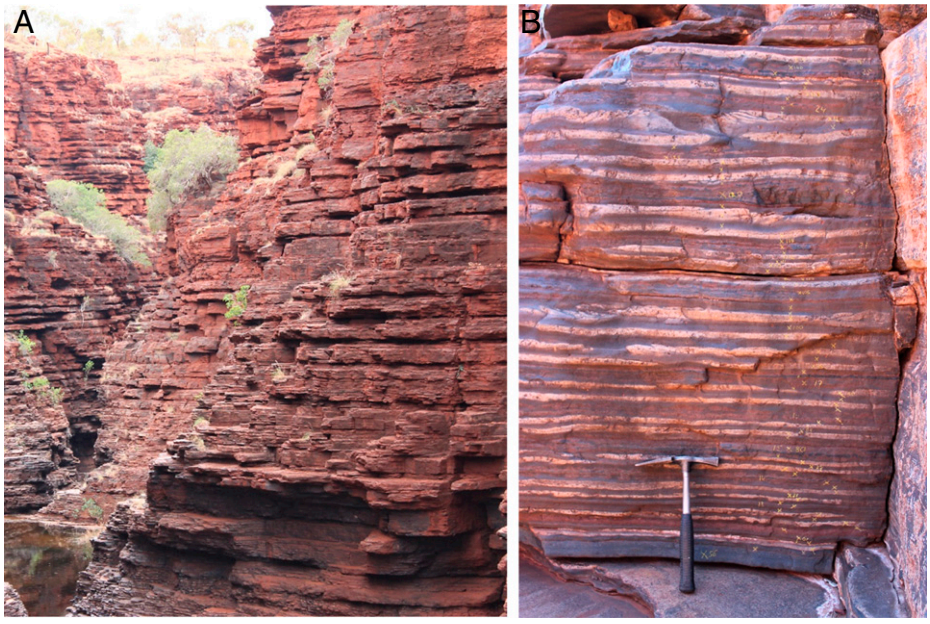

Fig. 1. Photographs of the Joffre Member at Joffre Falls. (*A*) Regular medium-scale alternations between more indurated BIF and more weathered shaley lithology with a thickness of ~85 cm. Note also the larger-scale variations in intensity of the shale weathering. The right foreground section is about 20 m thick and corresponds roughly to levels S9 to S31 in Fig. 2. (*B*) Regular small-scale alternations of ~10 cm (the "Knox cyclothem") defined by a double white chert alternating with red/blue chert. The thin shaley layer (shadowy interval) just below the thick blue band, close to the bottom of the hammer, corresponds to S31, and the thin shaley layer in the middle of the picture corresponds to S32.

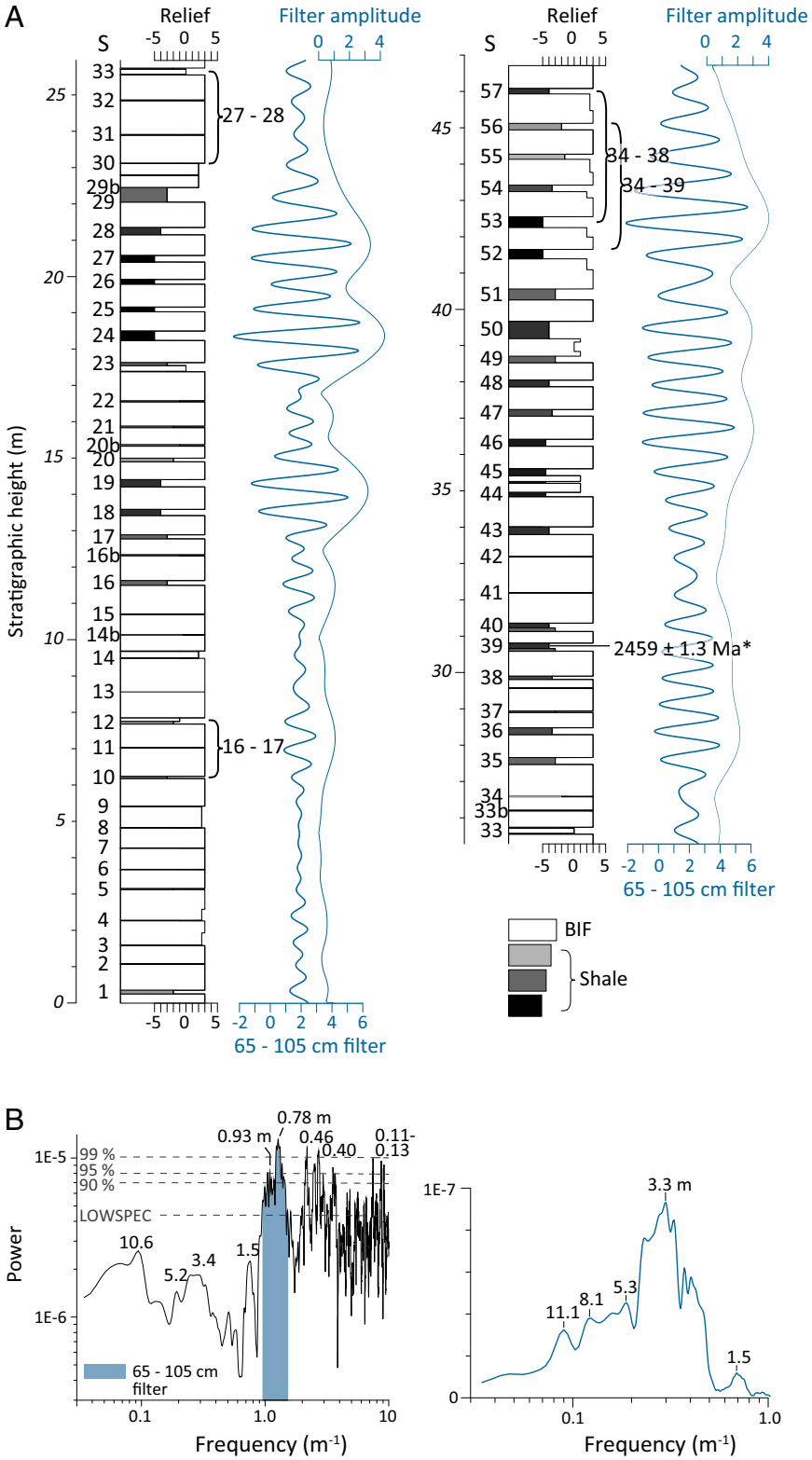

Fig. 2. (*A*) Composite log of the shale–BIF alternations at Joffre Falls and band-pass filters. "S" numbers on the left of the lithological columns mark the shaley intervals of individual ~85-cm alternations that occur on the interpreted scale of short (~100 ky) eccentricity; possible extra cycles that are relatively thinner are labeled "b." The rectangular black curve on the right-hand side of the columns represents the weathering profile, expressed in relief, with negative values corresponding to more weathered, shaley intervals and positive values to more indurated, BIF intervals. The thick blue curves represent the band-pass filtered (65 cm to 105 cm) relief signal, and the thin blue curve represents the amplitude modulation signal (Hilbert transform) of the band-pass filtered curve. The bracketed intervals indicate the positions of the three detailed logs and the corresponding minimum and maximum Knox cyclothem counts (see also Table 2). Asterisk (*) denotes CA-ID-TIMS zircon age from this study. (*B*) MTM power spectra for the (*Left*) relief record in *A* and (*Right*) amplitude modulation signal in *A*, with locally-weighted spectral (LOWSPEC) background and 90%, 95%, and 99% confidence level estimations, and peak labels in meters. The blue band in the left MTM spectrum highlights the 65- to 105-cm band-pass window corresponding to the filtered signal in *A*.

the outcrop scale. We logged the observed changes in lithology and relief for a total of 57 shale–BIF alternations (Fig. 2 and *SI Appendix*, Figs. S3 and S4).

Zooming in on the ∼85-cm alternations, we identified the consistent expression of small-scale alternations of ∼5 cm to 15 cm (Fig. 1*B*), matching Trendall's description of the Knox cyclothem (35). The alternations typically consist of 1) two white chert layers in a magnetite-rich matrix alternating with 2) a red chert layer centered within a dark greenish-gray, softer ("mixed") lithology. However, their expression and thickness can vary significantly within the larger-scale shale–BIF variability (Fig. 3*A* and *SI Appendix*). From the lower, middle, and upper parts of Joffre Falls, we selected three representative short stratigraphic intervals (Fig. 2*A* and *SI Appendix*, Fig. S5) for detailed logging of the small-scale Knox cyclothems, complemented by handheld measurements of color and X-ray fluorescence (XRF) (*SI Appendix*, Figs. S6 and S7 and Dataset S1). Of the acquired datasets, the lightness pattern, Si/Fe ratio, and K abundance (percent) appear to most accurately reflect the Knox cyclothem structure (Fig. 3*B*), with the K% signal additionally showing a clear amplitude modulation pattern of the cyclothems that follows the larger-scale shale–BIF cyclicity (Fig. 3*C*).

To statistically evaluate the described scales of alternations for periodicity and determine their wavelengths more precisely, we subsequently applied time series analysis. Multitaper method (MTM) (38) power spectra for the complete log show dominant peaks around 78 and 93 cm (Fig. 2*B* and *SI Appendix*, Fig. S8 *A* and *B*), exceeding 99% confidence levels (39), as well as the concentration of power around 1.5, 3 to 4, 5, 8, and 11 m corresponding to the observed bundling. The 78- and 93-cm cycles together define the basic ∼85-cm shale–BIF alternations as demonstrated by the band-pass filtered (65 cm to 105 cm) signal (Fig. 2 and *SI Appendix*, Fig. S9). The amplitude modulation of this signal reveals a dominant ∼3.3-m cycle (Fig. 2*B*, Table 1, and *SI Appendix*, Fig. S8*C*).

Spectral analysis of the geochemical records (Si/Fe and K%) from the three short intervals, however, produces very complex spectra, with multiple peaks in the 2- to 17-cm range (*SI Appendix*, Fig. S10). This complexity results from the variable thickness and the two to three (Si/Fe and/or K%) maxima per small-scale cycle, reflecting the characteristic double to triple occurrence of chert and/or mixed beds of the Knox cyclothem structure (*SI Appendix*, Fig. S11). To avoid these statistical complications in determining their mean period and ratio with the larger-scale shale–BIF cyclicity, we switched to the visual approach of counting the number of small-scale alternations per larger scale cycle for each of the short sections (*SI Appendix*). Including absolute uncertainties for intervals where the cycle

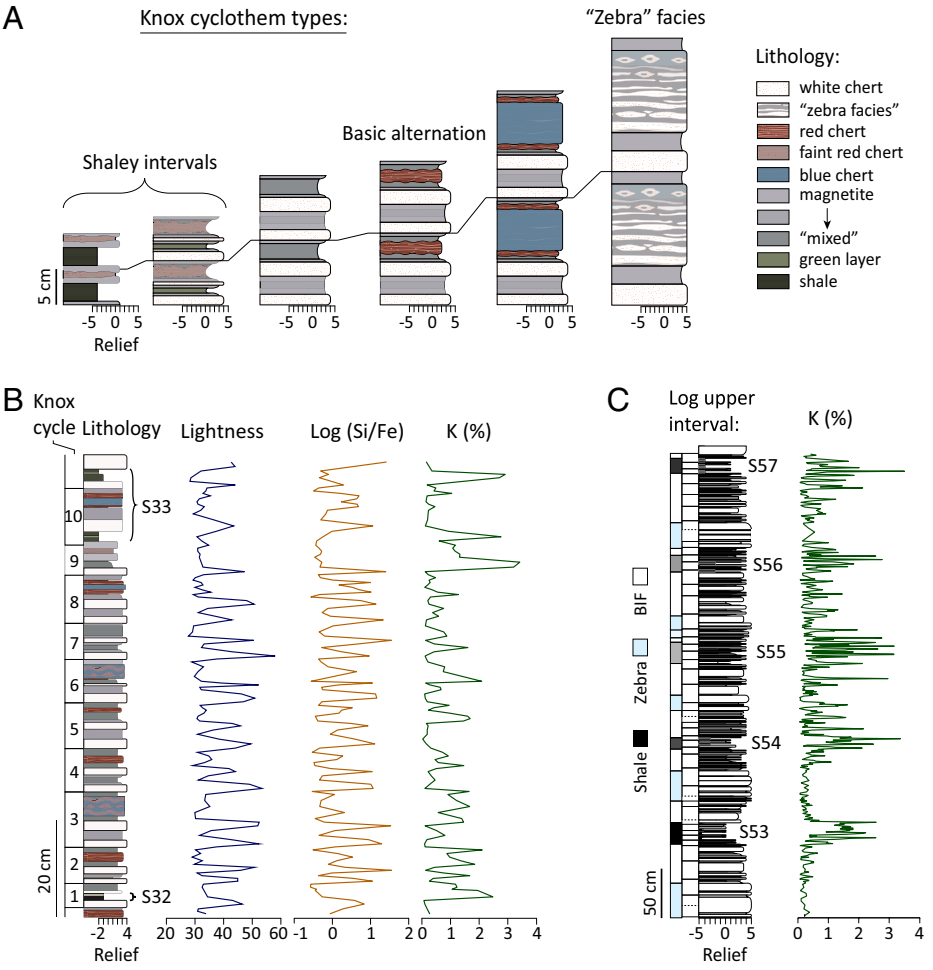

Fig. 3. Characterization of the small-scale "Knox cyclothem" alternations interpreted as climatic precession. (*A*) Schematic "idealized" representations of the different types of Knox cyclothems observed at Joffre Falls. Note the large range in their characteristic thickness. See main text and *SI Appendix* for a more detailed description. (*B*) Detailed lithological log with proxy data from the S32 to S33 interval of the middle interval (for complete record, see *SI Appendix*, Fig. S6). Counted Knox cyclothem cycle numbers are indicated on the left. Note that, per single cyclothem, there are, typically, two or three maxima in the lightness, Si/Fe, and K% records. (*C*) Simplified log of the upper interval showing clear amplitude variations of the small-scale cyclicity at the thickness scale of the medium-scale (∼85 cm) cycles, reflected in the K% record.

Table 1. Stratigraphic cycles at Joffre Falls identified from the large-scale log and their interpreted Milankovitch cycle origins

Lithological cycle name	Mean wavelength (m)	Long eccentricity-calibrated period* (ky)	Milankovitch cycle	Astronomical term(s)	Present-day period† (ky)
Medium-scale (~85 cm) shale–BIF cycles	0.78–0.93	95–113	~100-ky short eccentricity	$g_4 - g_5$, $g_3 - g_5$, $g_4 - g_2$, $g_3 - g_2$	95, 99, 124, 131
Large-scale modulating cycle	3.3	405	405-ky long eccentricity	$g_2 - g_5$	405
	5.3	643	690-ky very long eccentricity modulation	$g_2 - g_1$	688
	8.1	982	980-ky very long eccentricity modulation	$g_1 - g_5$	978
	11.1	1,346‡	"2.4-My" very long eccentricity modulation	$g_4 - g_3$	2,373

*Assuming 3.3 m = 405 ky.
†From ref. 12.
‡This cycle is tentatively linked to the ~2.4-My eccentricity cycle ($g_4 - g_3$), the period of which is unstable and can become much shorter (*SI Appendix*).

expression is relatively weak or condensed (*SI Appendix*, Fig. S7), we arrive at an average thickness of 8.9 ± 0.3 cm per Knox cyclothem and 8.9 ± 0.4 cyclothems per shale–BIF bundle, determined over a total of nine bundles (Table 2 and *SI Appendix*, Tables S1 and S2).

Uranium–Lead Dating and Milankovitch Interpretation. To establish a Milankovitch control and interpretation for the observed cycles at Joffre Falls, radioisotopic ages of sufficient accuracy and precision are required for independent calculation of the depositional rate and cycle periods. For this purpose, we have targeted multiple zircon-bearing shales from a drill core of the Joffre Member (core DD98SGP001) for chemical abrasion isotope dilution thermal ionization mass spectrometry (CA-ID-TIMS) U–Pb zircon dating (*SI Appendix* and Dataset S2). Fortunately, concordant, or close to concordant, analyses were obtained from four different shale intervals, all of which produced ages in agreement with stratigraphic superposition, with the lower- and upper-most levels giving ages of 2,469.1 ± 0.65 Ma (2σ) and 2,454.0 ± 0.62 Ma (2σ), respectively (Fig. 4*A*). Together, these U–Pb ages allow the calculation of a mean depositional rate of ~5 m/My to 15 m/My (Fig. 4*B*).

We also dated a zircon-rich shale layer from Joffre Falls itself (shale S39; Fig. 2) that yielded a concordant age of 2,459.2 ± 1.3 Ma, which places this section within the well-dated time window of the Joffre Member in the core (*SI Appendix*, Fig. S12). This implied correlation contradicts previous lithostratigraphic correlations (36, 37) that suggest that the Joffre Falls section corresponds to a stratigraphic level just above the core interval that has been used to establish a depositional rate (*SI Appendix*). Notwithstanding this slight disagreement in correlation, we consider it reasonable to invoke the depositional rate determined from the core for Joffre Falls, in particular, given that the same cycle hierarchy and small-scale cycle thickness were also observed in the core (*SI Appendix*). Furthermore, our new depositional rate estimate for the Joffre Member is identical to the previously established 10 m/My mean rate of the lithologically similar and coeval Kuruman IF in South Africa (33) and Dales Gorge Member ~50 m below the Joffre Member in the Brockman IF (33, 34).

Table 2. Summary of the small-scale (Knox cyclothem) counts and reconstructed period of climatic precession according to the different options

Interval	Number of medium-scale cycles	Number of small-scale cycles	Average per medium-scale cycle	Option 1 period* (ky)	Option 2a period† (ky) (2σ)	Option 2b period‡ (ky) (2σ)	Option 2a & 2b combined (2σ)
Lower (S10-12)	2	16–17	8.25 ± 0.25	10.9 ± 1.6	11.7 ± 1.4	12.0 ± 1.4	
Middle (S30-33)	3	27–28	9.17 ± 0.17	11.0 ± 1.3	10.5 ± 0.8	10.7 ± 0.9	
Upper (S53-57)	4	34–38	9.13 ± 0.63	10.7 ± 1.9§	10.7 ± 0.8	10.9 ± 1.0	
(Z52-56)¶	*4*	*34–39*	*9.00 ± 0.50*				
Total	9	77–84	8.94 ± 0.39	10.9 ± 1.7	10.8 ± 0.7	11 ± 0.7	10.9 ± 0.8#

*Based on the average thickness of the 405-ky eccentricity cycle (*SI Appendix*, Fig. S14) and the average thickness of the small-scale cycles for the respective intervals (*SI Appendix*, Table S2).
†Based on the average duration of short eccentricity for the respective intervals derived from the ref. 12 La2004 solution between 0 and 50 Ma (*SI Appendix*, Table S3) and the counted number of small-scale cycles.
‡Same as option 2a but using the ref. 45 ZB18a solution between 50 and 80 Ma.
§Value based on a thickness correction (*SI Appendix*, Table S2 and Fig. S13).
¶Alternative counting for the upper interval based on the major "zebra" intervals Z52 to Z56 (in italics). For complete counting procedures and uncertainties, see *SI Appendix*, *Supplementary Text* and Fig. S7.
#Selected value for determining the astronomical precession frequency p, following *SI Appendix*, Eq. S2.

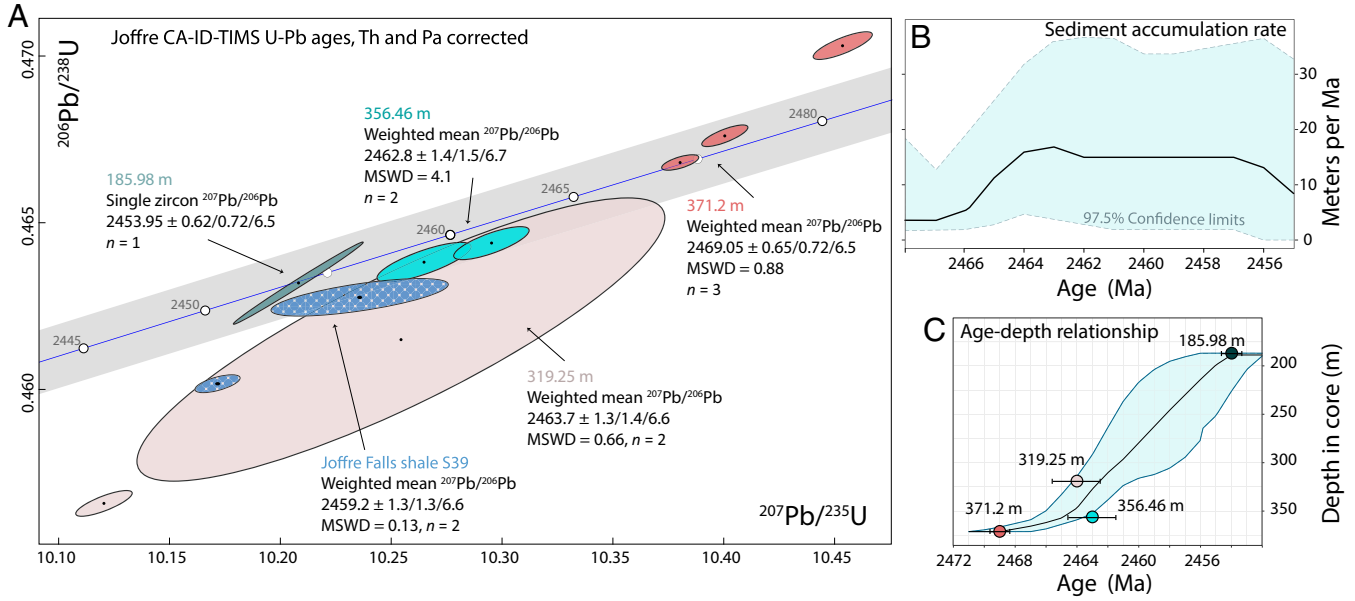

Fig. 4. U–Pb zircon ages and depositional rate. (*A*) Concordia diagram showing the concordant and close to concordant CA-ID-TIMS analyses and their resulting ages from the DD98SGP001 Joffre drill core samples (in solid colors, with associated sample depth) and also from shale S39 from Joffre Falls (stippled). The ellipses represent the U–Pb isotopic data and 2σ uncertainty for individual chemically abraded zircon fragments. The $^{207}Pb/^{206}Pb$ ages for each sample are presented as weighted mean ages with associated mean square of the weighted deviates (MSWD), or as individual zircon ages when only one concordant zircon was found. (*B*) Sediment accumulation rate for the Joffre drill core, with the 97.5% CIs indicated. (*C*) Age–depth model for the Joffre core showing the modeled age at each position along the core.

Combining the results from the cyclostratigraphic analysis and U–Pb dating, we can address the question of the astronomical origin of the Joffre Member cycles. The thickness ratio of ∼1:4 between the distinct medium-scale (78 cm to 93 cm) shale–BIF alternations and the main large-scale (∼3.3 m) cycle, coupled with their U–Pb calibrated periodicities, provide consistent evidence for the interpretation that these cycles are the expression of the short (∼100 ky) and long (405 ky) eccentricity cycles of Earth's orbit (*SI Appendix*). Assigning the 3.3-m cycle to the stable 405-ky eccentricity cycle converts the other longer-period amplitude modulation terms to periods that can be attributed to known longer-period eccentricity modulations (Table 1). Accordingly, the most logical explanation for the small-scale cycles (Knox cyclothems), given the implied eccentricity dominance, their thickness ratio of ∼1:9 (Table 2 and *SI Appendix*, Table S2), and their amplitude modulation by the short-eccentricity-related cycle (Fig. 3*C*), is that they represent the climatic precession cycle with a much-reduced period compared to the modern ∼21 ky, as expected for this time (8, 11, 13, 27).

Our precession interpretation for the Knox cyclothems is consistent with a low paleolatitude at the time of deposition of these sediments suggested by paleomagnetic reconstructions (40–42) and the absence of a clear obliquity signal. We also suggest that the characteristic double whitish chert bands that we observe per precession-related cycle are most likely of diagenetic origin, considering the internal build-up of the alternations (Figs. 1 and 3) and the resemblance to diagenetically controlled quadruplet cycles from the Pliocene (43). This implies that the presence of the two or three elemental and color maxima per small-scale cycle, which track the characteristic double to triple occurrence of chert and/or mixed beds in the Knox cyclothems (*SI Appendix*, Fig. S11), are of a diagenetic origin as well. Hence the associated high-frequency peaks in the spectra (*SI Appendix*, Fig. S10) likely do not represent a true climatic signal at the subprecessional scale (44), but rather are an artifact of the diagenetic structure of the cycles.

In conclusion, the cyclostratigraphic and U–Pb results from Joffre Falls are consistent with our initial Milankovitch hypothesis, namely, a climatic precession, and short and long eccentricity origin of the small-scale (∼9 cm), medium-scale (∼78 cm to 93 cm), and large-scale (∼3.3 m) cycles, respectively. With this confirmation, we can now proceed with the determination of the astronomical precession frequency p needed to reconstruct the Earth–Moon distance and LOD.

Reconstructing the Precession Period, Earth–Moon Distance, and LOD. To estimate the precession frequency p from the identified climatic precession signal, previous studies have employed methods that are based on the identification of spectral peaks associated with the individual astronomical (Milankovitch) cycle components, as determined from time series analysis of linearly tuned climate proxy records (26, 27, 29). Importantly, climatic precession is composed of various frequency components that are designated as combinations of the astronomical precession frequency p and one of the fundamental planetary g_i frequencies of planet i, which describe the rotation of a planet's elliptical orbit on its orbital plane ($p + g_i$). However, in our case, determining these individual components is not feasible given the large degree of stratigraphic distortion at the precession scale and the resultant variations in the thickness of the Knox cyclothems (Fig. 3 and *SI Appendix*, Fig. S10). We therefore followed an alternative stepwise approach in which we first determined the average period of climatic precession in the time domain, using the previously established mean thicknesses and/or ratios of the Knox cyclothems (Table 2 and *SI Appendix*, Table S2) with the long (option 1) or short (options 2a and b) eccentricity-related cycles, prior to the extraction of p.

In option 1, we converted the average Knox cyclothem thickness (8.9 ± 0.3 cm) to time by taking the mean wavelength (thickness) of the long-eccentricity-related cycle of 3.3 m, as determined by spectral analysis (Fig. 2*B*). This method has the clear advantage that long eccentricity is only composed of a single frequency component ($g_2 - g_5$) with a stable period of 405 ky (12, 22). This approach yields a mean climatic precession cycle period of 10.9 ± 1.7 ky (Table 2), which is consistent

between the three separate intervals (*SI Appendix*, Table S2). However, the disadvantage is the relatively large uncertainty in the 3.3-m wavelength (*SI Appendix*, Figs. S13 and S14).

Therefore, option 2a is used to calculate the average climatic precession period from the average number of precession-related Knox cycles per short-eccentricity-related bundle (8.9 ± 0.4). For this purpose, we need to know the average period of the short "100 ky" eccentricity cycle, which, in contrast to long eccentricity, is composed of four main components (Table 1). Determining the average short eccentricity period is not straightforward, because the time span between successive short eccentricity maxima varies considerably (≥12 ky) from one cycle to the next as seen in theoretical eccentricity solutions, due to the interference between individual cycle components (*SI Appendix*, Fig. S15). However, this variability is reduced, because we have looked at two, three, and four successive short eccentricity bundles in three different stratigraphic intervals. For this reason, we determined the average short eccentricity duration and associated uncertainty for comparable short intervals, that is, containing two, three, and four successive cycles, from the standard La2004 solution (12) between 0 and 50 Ma, using a Monte Carlo simulation approach (*SI Appendix*). This method (option 2a) yields an average duration of 96.2 ky (*SI Appendix*, Table S3 and Fig. S16) and an average climatic precession period of 10.8 ± 0.7 ky (Table 2 and *SI Appendix*, Table S2). The outcome is very similar to option 1, but it is more precise.

With option 2b, we repeated our exercise of option 2a, but using the ZB18a eccentricity solution (45) between 50 and 80 Ma instead. The main reason for selecting this interval in ZB18a is that it is marked by a shortening in the period of the very long ("2.4 My") eccentricity cycle ($g_4 - g_3$), down to ∼1.5 My to 1.6 My, owing to chaotic behavior in the solar system. Given that a similarly strong shortening of this cycle might have been the case during deposition of the Joffre Member (Table 1 and *SI Appendix*), it is important to check the effect of this change on the periods of the individual short eccentricity cycle components, as these are affected by changes in the period of $g_4 - g_3$. However, it turns out that this modified approach (option 2b) yields only a slight (2 ky) lengthening in the average period of short eccentricity (*SI Appendix*, Table S3), resulting in a very similar average climatic precession period of 11.0 ± 0.7 ky. The difference is minor because the changes in the frequencies of the four main ∼100-ky eccentricity components do not substantially change the average period of the short eccentricity cycle (*SI Appendix*, Fig. S17). Nevertheless, we prefer to incorporate this extra uncertainty in our calculation of the climatic precession period by combining the outcomes of options 2a and 2b. Accordingly, we arrive at an overall mean period for climatic precession of 10.9 ± 0.8 ky (Table 2).

Finally, to isolate the astronomical precession frequency p from the average climatic precession period, we assume that each of the four major climatic precession terms ($p + g_i$) contributes to the total average precession signal with a factor that scales to their relative amplitude (*SI Appendix*). This assumption seems valid, as we tested it on different intervals of the La2004 solution (*SI Appendix*, Table S4). For the calculation (*SI Appendix*, Eqs. S1 and S2), we used the present-day g_i frequencies and amplitudes of ref. 12, rather than trying to reconstruct these values from the inferred eccentricity-related cycles in the Joffre Falls record (Table 1), considering that their wavelengths are poorly constrained and highly sensitive to minor changes in sedimentation rate (Fig. 2*B* and *SI Appendix*, Figs. S9, S13, and S14). With this approach, we arrive at an astronomical precession frequency p of 108.6 ± 8.5 arcsec/y (period of 11.9 ± 0.9 ky), corresponding to an Earth–Moon distance of 321,800 ± 6,500 km and LOD of 16.9 ± 0.2 h (*SI Appendix*, Fig. S18). The application of the mean g_i frequency values established for 2.46 Ga based on ref. 22 yields essentially the same outcome (precession frequency p of 108.7 ± 8.5 arcsec/y) (*SI Appendix*). Note that, for this latter average, we use the present-day amplitudes of La2004 (12), as no amplitude values are provided in ref. 22.

Discussion

We compare our reconstructed Earth–Moon distance from the Joffre Member BIF to previous geological estimates from the Precambrian (16–19, 27, 46–50) to Cambrian (28, 29) and to a number of theoretical models (8, 13, 51, 52) in Fig. 5. First, we note that the Joffre Member datum for *ca.* 2.46 Ga indicates a noticeably shorter (10,000 km to 18,000 km) distance than suggested by the two tidalite-based estimates from the slightly younger Weeli Wolli Formation at *ca.* 2.45 Ga (Fig. 5*A*). However, the Weeli Wolli estimates are based on two fundamentally different interpretations of the same record, namely, 1) bundles of 23 microbands interpreted as annual layers modulated by the lunar nodal tide cycle (48) versus 2) bundles of 28 to 30 microbands interpreted as lunar fortnightly cycles grouped into solar years (16, 17). Thus, at least one of these interpretations must be incorrect, illustrating the large uncertainty involved in the Weeli Wolli reconstructions lacking independent control on sedimentation rate.

One older estimate for the Earth–Moon distance is available from the Archean (50) and is based on tidal rhythmites in the *ca.* 3.2-Ga Moodies Group in South Africa analyzed by ref. 49. Relative to the Joffre Member datum, the Moodies Group estimate points to a significant further reduction in the Earth–Moon distance with increasing age (Fig. 5*A*), a trend that is consistent with the expected direction of lunar orbital evolution through (geologic) time due to tidal dissipation in the Earth–Moon system (11, 51). Nevertheless, the Moodies Group estimate should be treated with caution, since a recent reevaluation of the tidal sequences indicates that the laminae counts of ref. 49 likely suffer from incomplete preservation (53). Also, it is unclear how ref. 50 determined an Earth–Moon distance from the information provided in ref. 49 (*SI Appendix*).

Estimates for the late Paleoproterozoic to Cambrian (Fig. 5*A*) are partly based on the Milankovitch cycle ratio approach (27–29), and partly on tidal rhythmites (16, 17, 46, 47) and stromatolite growth bands (18, 19). These results show a further increase of the Earth–Moon distance with time relative to the Joffre Member datum. In particular, when all Milankovitch-based estimates are combined, a consistent pattern emerges of progressive lengthening of the lunar orbit during the Proterozoic. This trend is less evident from the tidalite-based estimates, which generally have larger error bars and show a wider spread. The stromatolite-based reconstructions from refs. 18 and 19 at *ca.* 1.88 Ga to 2.0 Ga suggest a significantly larger Earth–Moon distance than indicated by the trend based on the Milankovitch cycle data. However, the patterns of (daily) growth increments in these stromatolite sequences have been considered discontinuous (18) and therefore may only provide maximum estimates for the LOD/Earth–Moon distance (15, 17, 18). These estimates are therefore considered less suitable for data–model comparison (54).

Theoretical models plotted in Fig. 5 range from very simple approximations (curves a, f, and e) to more advanced, physically based models (curves b, c, and d) for the lunar recession history.

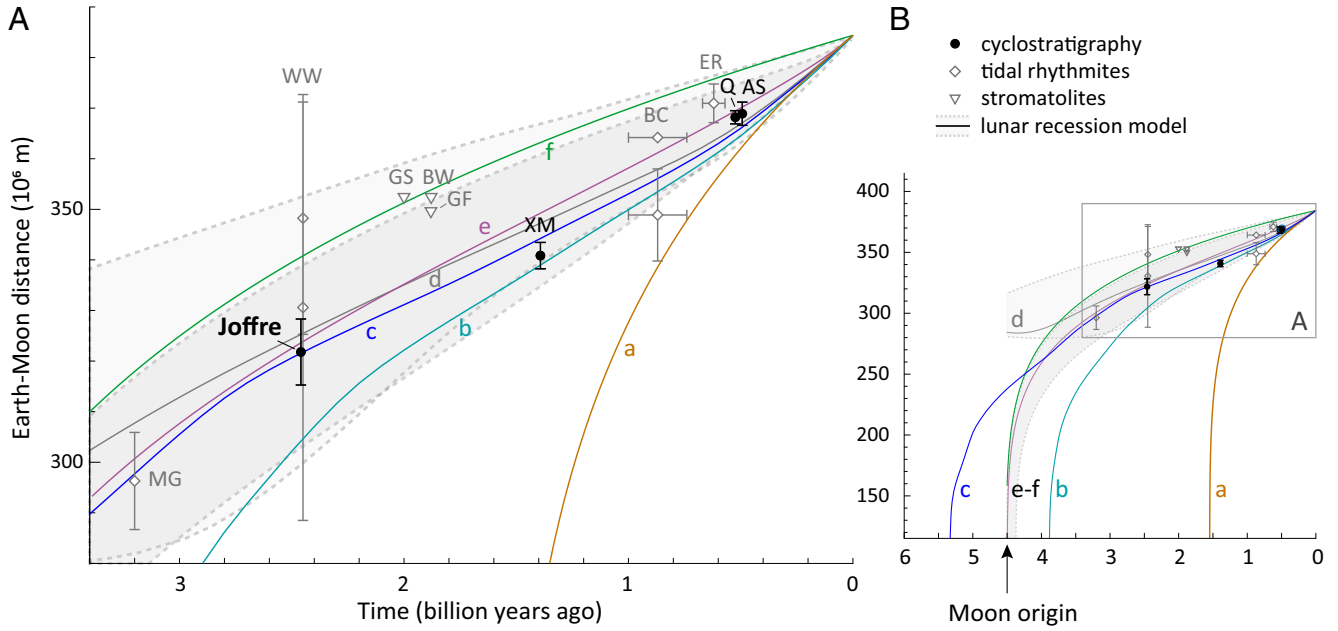

Fig. 5. Earth–Moon distance evolution through geologic time. Compilation of various geological data from the Precambrian to Cambrian and theoretical models for lunar recession history. (*A*) Geological reconstructions based on cyclostratigraphy are from the Joffre BIF at 2,459 ± 1.3 Ma (this study), the Xiamaling Formation (XM) (27), the Quongzhusi Formation (Q) (29), and Alum Shale (AS) (28). Reconstructions based on tidal laminae are from the Elatina-Reynella rhythmites (ER) (16, 17), two alternative estimates from the Big Cottonwood Formation (BC) (ref. 46 vs. ref. 47) and the Weeli Wolli Formation (WW) (ref. 17 vs. ref. 48), and the Moodies Group (MG) (49, 50). Stromatolite-based estimates are from the Great Slave Supergroup (GS) (18) and Gunflint (GF)–Biwabik (BW) Formations (18, 19) as reported in ref. 17. Vertical error bars are ±2σ. Age uncertainties represent maximum and minimum values; note that, for the Joffre, XM, and AS, these uncertainties fall within the size of the symbols. (*B*) Full trajectory of the Moon's recession history according to the different theoretical models for tidal dissipation: curve a is the "present-day rate" model and curve f is the "35% of the present-day rate" model as adapted from ref. 51; curves b and c are from the hemispherical ocean tide model of ref. 8 showing the evolution without (curve c) or including (curve b) a contribution from the solid Earth; curve e is the ocean model approximation of ref. 13 and the narrower gray band indicates the associated uncertainty; and curve d and the wider gray band are from the nonidealized ocean tide model of ref. 52 showing the evolution for a fixed present-day paleogeography (curve d) and varying paleogeography (wider gray band). Note that curves a through d violate the Moon formation age of *ca.* 4.5 Ga, while curves e and f were fitted to this age. See *SI Appendix, Supplementary Text* and Table S5 for plotting data.

Most geological estimates and none of the Milankovitch-based estimates are consistent with the simple "present-day rate" and "35% of present-day rate" curves a and f, respectively, adapted from ref. 51. More specifically, curve f is based on a constant tidal dissipation quality factor corresponding to an initial tidal dissipation rate that is about 35% of the present-day value. This model satisfies the *ca.* 4.5-Ga age of lunar formation, in contrast to the 100% rate scenario demonstrated by curve a (Fig. 5*B*), but violates the present-day lunar recession rate.

Instead, the Joffre Member datum and long-term trend suggested by the Milankovitch data show overlap with the "ocean model" curves b and c (8), d (52), and/or e (13). Compared to curve f, the ocean tide model curves of ref. 8 and the ocean model approximation of ref. 13 feature relatively higher rates of tidal dissipation in the most recent geologic history, versus overall lower rates of tidal dissipation and, correspondingly, a reduced rate of lunar recession in the distant past (Fig. 5*A*). This general trend, found in ref. 8 and other ocean tide model studies based on idealized basin geometries (9, 55), is attributed to the nonlinear tidal dissipation dependence on Earth's spin rate, inducing resonant stages where the tidal dissipation is greatly enhanced (55–58). However, the ocean model of ref. 8, shown in curve c, violates the formation age of the Moon and the solar system, implying an age of *ca.* 5.3 Ga (Fig. 5*B*). With curve b in Fig. 5, a contribution from the solid Earth tides was included (8), in this case resulting in an age of formation of the Moon of *ca.* 3.9 Ga. Ref. 52 used more complex (nonidealized) ocean basin geometries and observed a large effect of paleogeography (wider gray band in Fig. 5) as well as Earth rotation rate on past tidal dissipation and lunar orbital evolution. Curve d, which fits the Joffre Member estimate within uncertainty, represents the "unrealistic" scenario of a constant present-day basin geometry throughout Earth's history (52). Like model c of ref. 8, the simulations of ref. 52 result in a too large (i.e., nonzero) Earth–Moon distance at 4.5 Ga.

It is currently premature to draw firm conclusions from the comparisons between the geological estimates and the various modeling approaches, given the scarcity of geological data points thus far and the limitations of existing lunar recession models. In particular, the near-perfect match between our Joffre BIF estimate and the ocean model of ref. 8 is likely coincidental considering the uncertainty on the Joffre mean value, the simplified assumptions of ref. 8, and its violation of the Moon age. As emphasized in ref. 8, a limitation of this model could be the use of a flat-bottomed, 4.4-km-deep hemispherical ocean and a linear bottom friction term, since the magnitude of global oceanic tidal dissipation has been shown to be highly sensitive to (past changes in) ocean basin depth, shelf area, seafloor topography/roughness, and continental configuration (8, 13, 14, 51, 55–59). Recent efforts to model the influence of such paleogeographic variations over Earth's history have resulted in a wide range of possible trajectories for the lunar recession (52) (Fig. 5). In addition, changes in the relative contribution of the solid Earth tides, such as considered by ref. 8, might have played an additional role during, particularly, the earliest stages of the Earth–Moon system history (60).

Hence, additional reliable and precise data points from the Precambrian are needed to better constrain the trajectory of lunar retreat, including any superimposed variations arising

from frequency-resonant behavior and/or changes in paleogeography. A promising candidate for expanding our result from the Joffre Member are the potentially precession-scale (33, 34) Calamina cyclothems reported in certain intervals of the slightly older Dales Gorge Member of the Brockman IF, Western Australia (35), from which a preliminary estimate of 8 ky to 12 ky has already been published by ref. 34. Well-constrained cyclostratigraphic data combined with estimates of high-quality tidalites from the Proterozoic are further needed as a test for more speculative models that propose a constant 21-h daylength due to resonance locking by the atmospheric thermal tide (54, 61, 62) and/or extreme changes in dynamical ellipticity associated with Snowball Earth events (63). Since major BIFs were formed back to 3.8 Ga (32), these deposits are potential candidates for reconstructing Earth–Moon system evolution during more distant (Archean) time intervals when ocean basin geometry and solid Earth tidal dissipation may have been very different.

In summary, our study on the reconstruction of Earth's precession frequency based on the 2.46-Ga Joffre Member presents the oldest reliable datum currently available for constraining the dynamical history of the Earth–Moon system. It is based on an integrated cyclostratigraphic approach, independently verified by high-precision U–Pb ages, and is therefore considered to be more robust than previous approaches based on tidalites and fossil growth increments. We anticipate that our established value for the precession frequency (and associated Earth–Moon distance and/or daylength) will serve as an important reference point for comparison with improved modeling in the future (64).

Materials and Methods

Cyclostratigraphic Analyses. From the outcrops of the Joffre Member within the Karijini National Park, a ∼47-m interval at Joffre Falls was selected for logging of the regular shale–BIF alternations and the development of a ranked relief record of the associated changes in weathering profile. From a lower, a middle, and an upper part, three short intervals were selected for logging of the small-scale alternations where these were particularly clear, complemented by nondestructive color and XRF analysis for which we targeted the freshest rock exposures close to the waterfall. MTM power spectral analysis (using a time-bandwidth product of three), band-pass filtering (using a rectangular window), and Hilbert transform analyses were carried out on linearly detrended and interpolated records using the functions in Astrochron (65). See *SI Appendix* for a full description of the methodology, including cycle counting procedures.

TIMS U–Pb Geochronology. High-precision, CA-ID-TIMS U–Pb zircon ages were generated from zircon-rich shale horizons within the Joffre Member from both drill core DD98SGP001 and shale S39 at Joffre Falls. All shales were analyzed for their Zr concentrations using a handheld XRF device prior to zircon extraction. Hand-picked idiomorphic zircon crystals from the Zr-rich shale layers were chemically abraded to remove the effect of decay damage–related Pb loss and then dated using CA-ID-TIMS techniques outlined in ref. 33 and described in *SI Appendix*. The ages reported here are weighted mean or single-crystal $^{207}Pb/^{206}Pb$ ages from concordant or close to concordant zircon analyses (Fig. 4 and *SI Appendix*, Fig. S12).

Determining Earth's Precession Frequency. The results of options 2a and 2b were combined to arrive at a mean period for the climatic precession cycle (see Reconstructing the Precession Period, Earth-Moon Distance, and LOD and Table 2). The astronomical precession frequency p was subsequently extracted using the approximation: frequency (freq.) p = freq. mean climatic precession − (amplitude fraction g_5 * freq. g_5 + amplitude fraction g_2 * freq. g_2 + amplitude fraction g_4 * freq. g_4 + amplitude fraction g_3 * freq. g_3) (see *SI Appendix*, Eq. 1 and 2). Earth–Moon distance and LOD were estimated from p following the method of ref. 27. A complete explanation of the approach, and determination and propagation of errors, is given in *SI Appendix*.

Data, Materials, and Software Availability. All study data are included in the article and/or supporting information.

ACKNOWLEDGMENTS. We thank the Geological Survey of Western Australia and D. Martin for logistical support during two field campaigns (2018–2019), and G. Jack and P. Mason for help with the XRF and colorimetric scanning. R. Ray is acknowledged for sharing the original data of D. Webb's model, and D. Waltham is acknowledged for sharing his model calculation sheet. We are grateful to the reviewers and PNAS editor for constructive comments. We are grateful to M. Farhat, P. Auclair-Desrotour, J. Laskar, and coworkers for advice on the geophysical/tidal aspects, and to M. Sinnesael and G. Halverson for proofreading. This study was funded by the Dutch National Science Foundation (Grant NWO ALWOP.192), the Swiss National Science Foundation (Grant 200021_169086), and the Natural Sciences and Engineering Research Council of Canada (Grant RGPIN-2019-07078). M.L.L. and F.J.H. acknowledge support from the Dr. Schürmann Foundation (Grants 2018-136 and 2019-145).

Author affiliations: [a]Department of Earth Sciences, Utrecht University, Utrecht, 3584 CB The Netherlands; [b]Department of Earth Sciences, University of Geneva, CH-1205 Geneva, Switzerland; and [c]Département des sciences de la Terre et de l'atmosphère/Geotop, Université du Québec à Montréal, Montréal, QC H2X 3Y7, Canada

1. G. H. Darwin, On the secular changes in the elements of the orbit of a satellite revolving about a tidally distorted planet. *R. Soc. London. Philos. Trans.* **171**, 713–891 (1880).
2. N. H. Gerstenkorn, The earliest past of the Earth–Moon system. *Icarus* **11**, 189–207 (1969).
3. J. O. Dickey *et al.*, Lunar laser ranging: A continuing legacy of the Apollo Program. *Science (80-.)* **265**, 482–490 (1994).
4. T. Kleine, H. Palme, K. Mezger, A. N. Halliday, Hf-W chronometry of lunar metals and the age and early differentiation of the Moon. *Science (80-.).* **310**, 1671–1674 (2005).
5. M. Touboul, T. Kleine, B. Bourdon, H. Palme, R. Wieler, Late formation and prolonged differentiation of the Moon inferred from W isotopes in lunar metals. *Nature* **450**, 1206–1209 (2007).
6. M. Barboni *et al.*, Early formation of the Moon 4.51 billion years ago. *Sci. Adv.* **3**, e1602365 (2017).
7. W. Munk, Once again–Tidal friction. *Q. J. R. Astron. Soc.* **9**, 352 (1968).
8. J. Webb, Tides and the evolution of the Earth-Moon system. *Geophys. J. R. Astron. Soc.* **70**, 261–271 (1982).
9. K. S. Hansen, Secular effects of oceanic tidal dissipation on the Moon's orbit and the Earth's rotation. *Rev. Geophys. Space Phys.* **20**, 457–480 (1982).
10. A. Berger, M. F. Loutre, J. Laskar, Stability of the astronomical frequencies over the Earth's history for paleoclimate studies. *Science* **255**, 560–566 (1992).
11. A. Berger, M. F. Loutre, P. L. De Boer, D. G. Smith, "Astronomical forcing through geological time" in *Orbital Forcing and Cyclic Sequences*, P. L. de Boer, D. G. Smith, Eds. (Blackwell Scientific, Oxford, 1994), pp. 15–24.
12. J. Laskar *et al.*, A long-term numerical solution for the insolation quantities of the Earth. *Astron. Astrophys.* **428**, 261–285 (2004).
13. D. Waltham, Milankovitch period uncertainties and their impact on cyclostratigraphy. *J. Sediment. Res.* **85**, 990–998 (2015).
14. J. A. M. Green, M. Huber, D. Waltham, J. Buzan, M. Wells, Explicitly modelled deep-time tidal dissipation and its implication for Lunar history. *Earth Planet. Sci. Lett.* **461**, 46–53 (2017).
15. K. Lambeck, *The Earth's Variable Rotation* (Cambridge University Press, 1980).
16. G. E. Williams, Late Precambrian tidal rhythmites in South Australia and the history of the Earth's rotation. *J. Geol. Soc. London* **146**, 97–111 (1989).
17. G. E. Williams, Geological Constraints on the Precambrian History of Earth's Rotation and the Moon's Orbit. *Rev. Geophys.* **38**, 37–59 (2000).
18. G. Pannella, Paleontological evidence on the Earth's rotational history since early Precambrian. *Astrophys. Space Sci.* **16**, 212–237 (1972a).
19. G. Pannella, "Precambrian stromatolites as paleontological clocks" in *24th International Geological Congress*, James E. Gill, Ed. (International Geological Congress, 1972), pp. 50–57.
20. J. Laskar, A. Fienga, M. Gastineau, H. Manche, La2010: A new orbital solution for the long term motion of the Earth. *Astron. Astrophys.* **532**, A89 (2011).
21. P. E. Olsen *et al.*, Mapping solar system chaos with the geological orrery. *Proc. Natl. Acad. Sci. U.S.A.* **116**, 10664–10673 (2019).
22. N. H. Hoang, F. Mogavero, F. J. Laskar, Chaotic diffusion of the fundamental frequencies in the Solar System. *Astron. Astrophys.* **654**, A156 (2021).
23. F. J. Hilgen *et al.*, Stratigraphic continuity and fragmentary sedimentation: The success of cyclostratigraphy as part of integrated stratigraphy. *Geol. Soc. Lond. Spec. Publ.* **404**, 157–197 (2015).
24. L. J. Lourens, R. Wehausen, H. J. Brumsack, Geological constraints on tidal dissipation and dynamical ellipticity of the Earth over the past three million years. *Nature* **409**, 1029–1033 (2001).
25. C. Zeeden, F. J. Hilgen, S. K. Hüsing, L. J. Lourens, The Miocene astronomical time scale 9 – 12 Ma: New constraints on tidal dissipation and their implications for paleoclimatic investigations. *Paleoceanography* **29**, 296–307 (2014).
26. H. Wu *et al.*, Time-calibrated Milankovitch cycles for the late Permian. *Nat. Commun.* **4**, 2452 (2013).
27. S. R. Meyers, A. Malinverno, Proterozoic Milankovitch cycles and the history of the solar system. *Proc. Natl. Acad. Sci. U.S.A.* **115**, 6363–6368 (2018).
28. A. L. Sørensen *et al.*, Astronomically forced climate change in the late Cambrian. *Earth Planet. Sci. Lett.* **548**, 116475 (2020).

29. T. Zhang *et al.*, Orbitally-paced climate change in the early Cambrian and its implications for the history of the Solar System. *Earth Planet. Sci. Lett.* **583**, 117420 (2022).
30. R. E. Zeebe, L. J. Lourens, A deep-time dating tool for paleo-applications utilizing obliquity and precession cycles: The role of dynamical ellipticity and tidal dissipation. *Paleoceanogr. Paleoclimatol.* **37**, e2021PA004349 (2022).
31. S. Zhang *et al.*, Orbital forcing of climate 1.4 billion years ago. *Proc. Natl. Acad. Sci. U.S.A.* **112**, E1406–E1413 (2015).
32. C. Klein, Some Precambrian banded iron-formations (BIFs) from around the world: Their age, geologic setting, mineralogy, metamorphism, geochemistry, and origin. *Am. Mineral.* **90**, 1473–1499 (2005).
33. M. L. Lantink, J. H. F. L. Davies, P. R. D. Mason, U. Schaltegger, F. J. Hilgen, Climate control on banded iron formations linked to orbital eccentricity. *Nat. Geosci.* **12**, 369–374 (2019).
34. P. de Oliveira Carvalho Rodrigues, L. A. Hinnov, D. R. Franco, A new appraisal of depositional cyclicity in the Neoarchean-Paleoproterozoic Dales Gorge Member (Brockman Iron Formation, Australia). *Precambrian Res.* **328**, 27–47 (2019).
35. A. F. Trendall, J. B. Blockley, *The Iron Formations of the Precambrian Hamersley Group, Western Australia with Special Reference to the Associated Crocidolite* (Geological Survey of Western Australia, 1970).
36. A. F. Trendall, "The Joffre Member in the Gorges South of Wittenoom" in *Geological Survey of Western Australia Annual Report for the year 1968* (Geological Survey of Western Australia, 1969), pp. 53–57.
37. A. L. Pickard, SHRIMP U-Pb zircon ages of tuffaceous mudrocks in the Brockman Iron Formation of Hamersley Range, Western Australia. *Aust. J. Earth Sci.* **49**, 491–507 (2002).
38. D. J. Thomson, Spectrum estimation and harmonic analysis. *Proc. IEEE* **70**, 1055–1096 (1982).
39. S. R. Meyers, Seeing red in cyclic stratigraphy: Spectral noise estimation for astrochronology. *Paleoceanography* **27**, PA3228 (2012).
40. M. O. de Kock, D. A. D. Evans, N. J. Beukes, Validating the existence of Vaalbara in the Neoarchean. *Precambrian Res.* **174**, 145–154 (2009).
41. A. P. Gumsley *et al.*, Timing and tempo of the Great Oxidation Event. *Proc. Natl. Acad. Sci. U.S.A.* **114**, 1811–1816 (2017).
42. Y. Liu *et al.*, Archean geodynamics: Ephemeral supercontinents or long-lived supercratons. *Geology* **49**, 794–798 (2021).
43. A. A. M. van Hoof *et al.*, A paleomagnetic and geochemical record of the upper Cochiti reversal and two subsequent precessional cycles from Southern Sicily (Italy). *Earth Planet. Sci. Lett.* **117**, 235–250 (1993).
44. A. Berger, M. F. Loutre, J. L. Mélice, Equatorial insolation: From precession harmonics to eccentricity frequencies. *Clim. Past* **2**, 131–136 (2006).
45. R. E. Zeebe, L. J. Lourens, Solar System chaos and the Paleocene–Eocene boundary age constrained by geology and astronomy. *Science (80-.)* **365**, 926–929 (2019).
46. A. C. P. Sonett, A. Zakharian, E. P. Kvale, A. Rinfret, Ancient tides and length of day: Correction. *Science (80-.)* **274**, 1068–1069 (1996).
47. C. P. Sonett, M. Chan, Neoproterozoic Earth-Moon dynamics: Rework of the 900 Ma Big Cottonwood Canyon tidal laminae. *Geophys. Res. Lett.* **25**, 539–542 (1998).
48. J. C. G. Walker, K. J. Zahnle, Lunar nodal tide and distance to the Moon during the Precambrian. *Nature* **320**, 600–602 (1986).
49. K. A. Eriksson, E. L. Simpson, Quantifying the oldest tidal record: The 3.2 Ga Moodies Group, Barberton greenstone belt, South Africa. *Geology* **28**, 831–834 (2000).
50. V. L. L. de Azarevich, M. B. Azarevich, Lunar recession encoded in tidal rhythmites: A selective overview with examples from Argentina. *Geo-Mar. Lett.* **37**, 333–344 (2017).
51. B. G. Bills, R. D. Ray, Lunar orbital evolution: A synthesis of recent results. *Geophys. Res. Lett.* **26**, 3045–3048 (1999).
52. H. Daher *et al.*, Long-term Earth-Moon evolution with high-level orbit and ocean tide models. *J. Geophys. Res. Planets.* **126**, e2021JE006875 (2021).
53. C. Heubeck *et al.*, Reassessing evidence of Moon–Earth dynamics from tidal bundles at 3.2 Ga (Moodies Group, Barberton Greenstone Belt, South Africa). *Sedimentology* **69**, 2025–2028 (2022).
54. J. M. Klatt, A. Chennu, B. K. Arbic, B. A. Biddanda, G. J. Dick, Possible link between Earth's rotation rate and oxygenation. *Nat. Geosci.* **14**, 564–570 (2021).
55. B. A. Kagan, N. B. Maslova, A stochastic model of the Earth-Moon tidal evolution accounting for cyclic variations of resonant properties of the ocean: An asymptotic solution. *Earth Moon Planets* **66**, 173–188 (1994).
56. M. S. Longuet-Higgins, G. S. Pond, The free oscillations of fluid on a hemisphere bounded by meridians of longitude. *Philos. Trans. R. Soc. Lond. Ser. A Math. Phys. Sci.* **266**, 193–223 (1970).
57. P. Auclair-Desrotour *et al.*, Oceanic tides from Earth-like to ocean planets. *Astron. Astrophys.* **615**, A23 (2018).
58. R. H. Tyler, On the tidal history and future of the Earth–Moon orbital system. Plan. *Sci. J.* **2**, 70 (2021).
59. B. W. Blackledge, J. A. M. Green, R. Barnes, M. J. Way, Tides on other earths: Implications for exoplanet and Palaeo-tidal simulations. *Geophys. Res. Lett.* **47**, e2019GL085746 (2020).
60. M. N. Ross, G. Schubert, Evolution of the lunar orbit with temperature-and frequency-dependent dissipation. *J. Geophys. Res. Solid Earth* **94**, 9533–9544 (1989).
61. B. C. Bartlett, D. J. Stevenson, Analysis of a Precambrian resonance-stabilized day length. *Geophys. Res. Lett.* **43**, 5716–5724 (2016).
62. K. Zahnle, J. C. G. Walker, A constant daylength during the Precambrian era? *Precambrian Res.* **37**, 95–105 (1987).
63. R. N. Mitchell *et al.*, Orbital forcing of ice sheets during snowball Earth. *Nat. Commun.* **12**, 4187 (2021).
64. M. Farhat, P. Auclair-Desrotour, G. Boué, J. Laskar, The resonant tidal evolution of the Earth-Moon distance. *Astron. Astrophys.* **665**, L1 (2022).
65. S. R. Meyers, An R package for astrochronology, Version 0.9. cran.rproject.org/web/packages/astrochron/index.html. Accessed 8 January 2019.